

Non-Contiguous Wi-Fi Spectrum for ISAC: Impact on Multipath Delay Estimation

Ana Jeknić, *Graduate Student Member, IEEE*, Aleš Švigelj, *Senior Member, IEEE*, Tomaž Javornik, *Senior Member, IEEE*, and Andrej Hrovat, *Senior Member, IEEE*

Abstract—Leveraging channel state information from multiple Wi-Fi bands can improve delay resolution for ranging and sensing when a wide contiguous spectrum is unavailable. However, frequency gaps shape the delay response, introducing sidelobes and secondary peaks that can obscure closely spaced multipath components. This paper examines multipath delay estimation for Wi-Fi-compliant multiband configurations using channel state information (CSI). For a two-path model with unknown complex gains and delays, the Cramér-Rao lower bound (CRLB) for delay separation is derived and analyzed, confirming the benefit of larger frequency aperture, while revealing pronounced, separation-dependent oscillations driven by gap geometry and inter-path coupling. Given the local nature of Cramér-Rao lower bound, the delay response is analyzed next. In the single-path case, the combined subband responses determine how delay-domain sidelobe levels are distributed. The dominant peak spacing is set primarily by the separation between subband center frequencies. In the two-path case, increased aperture sharpens the mainlobe but also intensifies sidelobes and leakage, yielding competing peaks and, in some regimes, a dominant peak shifted from the true delay. Finally, a normalized leakage metric is introduced to predict problematic separations and to identify regimes where local Cramér-Rao lower bound analysis does not capture practical peak-leakage behavior in delay estimation.

Index Terms—multiband sensing, multipath delay estimation, Cramér-Rao lower bound (CRLB), delay-domain sidelobes, channel state information (CSI), integrated sensing and communication (ISAC), multi-link operation (MLO)

I. INTRODUCTION

WIRELESS sensing systems built on communication-centric standards inherit the spectrum access rules, radio front-end (RF) constraints, and signal structures of those standards. High-resolution sensing benefits from large bandwidth or frequency aperture, but practical devices often operate over fragmented, non-contiguous allocations due to regulatory constraints and standard-defined channelization. To cope with this, modern wireless standards are therefore heading towards multiband operation [1]–[3]. For example, IEEE 802.11be (Wi-Fi 7) has already introduced this as multi-link operation (MLO) that enables channel aggregation across the 2.4, 5, and 6 GHz bands [4], while the forthcoming IEEE 802.11bn (Wi-Fi 8) continues multiband and multi-link operation (MLO) approach [5].

Multiband sensing in integrated sensing and communication (ISAC) systems jointly processes channel state information (CSI) from non-contiguous channels or bands to synthesize a larger effective bandwidth and improve delay resolution [6]–[9]. Since many localization and environment-characterization tasks ultimately rely on resolving propagation delays, a key

question is how multiband and non-contiguous spectrum impacts the estimation of these parameters.

Fig. 1 illustrates a representative indoor Wi-Fi sensing scenario. The link between an access point (AP) and a user is typically multipath, consisting of a line-of-sight (LoS) and non-line-of-sight (NLoS) components with delays and complex gains. In orthogonal frequency division multiplexing (OFDM) based standards, the channel is observed through CSI that consists of discrete channel frequency response (CFR) samples on the occupied subcarriers. In a multiband setting, each communication link may simultaneously occupy several disjoint Wi-Fi channels or bands, so CSI measurements are collected over non-contiguous frequency allocations that are subsequently fused to improve sensing resolution.

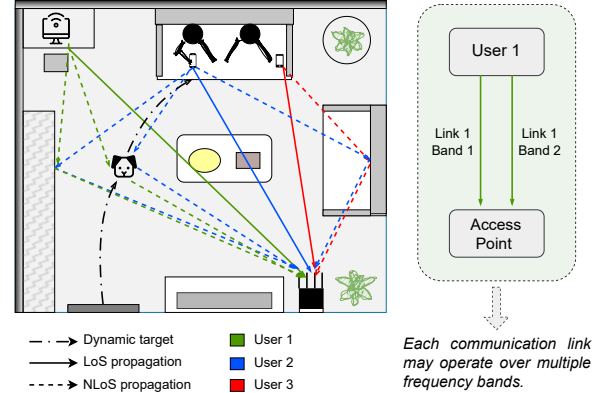


Fig. 1. Illustration of Indoor Multipath Propagation for Multiband WiFi Sensing.

Although a larger frequency aperture of multiband suggests improved delay resolution, non-contiguity creates a structured spectral window whose delay response exhibits sidelobes. In multipath conditions, these sidelobes can produce competing deterministic peaks, so performance may deviate from what aperture alone would suggest. Building on prior characterization of channel impulse response (CIR) broadening and error trends under non-contiguous spectrum [10], we provide an analytical treatment of multipath delay estimation for non-contiguous Wi-Fi allocations by combining Cramér-Rao lower bound analysis with sidelobe/leakage behavior induced by spectral gaps.

The main contributions of this work are as follows:

- A Wi-Fi-compliant multiband CSI/CFR model is formulated that accounts for non-contiguous channel aggrega-

tion, incorporating standard-defined specifications and enabling consistent comparison across different aggregation patterns.

- Cramér-Rao lower bound is derived for estimating the delays of closely spaced multipath components under non-contiguous spectral allocations, with a systematic analysis of accuracy dependence on total used bandwidth and effective aperture, gap geometry, signal-to-noise ratio (SNR) and multipath separation.
- The deterministic sidelobe structure induced by spectral gaps is derived from the multiband spectral window and summarized via a normalized leakage metric. This enabled prediction of path separations prone to competing deterministic peaks and regimes in which CRLB bound do and do not reflect practical performance.

The remainder of the paper is organized as follows. Section II places this work in relation to the relevant literature. Section III introduces the channel and observation models, formulates the problem, and defines the multiband Wi-Fi scenarios used throughout the paper. Section IV derives and analyzes the CRLB for a representative two-path case, emphasizing resolvability as a function of path separation. Section V then investigates the delay-domain structure induced by spectral gaps and discusses how it relates to the effects observed in practice. Finally, Section VI concludes the article and outlines directions for future work.

II. RELATED WORKS

Prior research on Wi-Fi sensing and localization includes CSI-based sensing pipelines, indoor positioning methods, and physical-layer analyses of resolvability under practical spectrum constraints. Many sensing systems are evaluated through inference tasks such as presence, motion and activity recognition, but their discriminative content still derives from how multipath superposition reshapes CSI [11]. Physics or channel model based feature design has also been explored to improve robustness in CSI-based classification, for example, for sensing LoS perturbations in 6-GHz Wi-Fi [12]. To improve robustness beyond a single link, some systems also leverage diversity across access points and antennas by forming multi-view CSI representations. For example, the multi-AP CSI fusion framework in [13] enhances the robustness of behavioral sensing under channel dynamics. Recent standardization for sensing in IEEE 802.11bf further supports cross-band operation as a practical direction for sensing deployment to improve reliability compared to single-band systems [14].

Together, these developments indicate that multiband operation can improve sensing and localization by expanding frequency diversity and, potentially, effective delay resolution. However, it also raises practical questions of inter-/intra-band coherence and calibration, and, less explicitly addressed, how standardized spectral gaps reshape the delay-domain response and ambiguity structure. Accordingly, this section groups the literature into: (i) multiband sensing under non-contiguous spectrum, including practical challenges and performance-limit analyses, and (ii) approaches for multipath delay estimation and the interpretation of bounds.

A. Multiband Sensing Under non-Contiguous Spectrum

Multiband sensing, also referred to as multiband splicing [15], [16], aims to combine channel measurements collected over several separated frequency allocations to emulate a wider effective bandwidth. In the delay domain, this fusion targets wideband-like channel characterization, either through CIR reconstruction or parametric estimation of multipath components (such as path delays and complex gains), with ToA estimation as a central special case for ranging and sensing. In this context, related work can be broadly grouped into several categories.

One line of work examines coherence as the main enabler of multiband fusion. In bistatic sensing, independent TX/RX oscillators and unsynchronized chains already induce phase and timing offsets [17], while multiband sensing adds the requirement of consistent inter-band phase across separated allocations. These issues are highlighted in [7] and surveyed in [15], emphasizing phase-offset compensation, RF impairment mitigation, and coherence-time constraints.

Another direction focuses on representative algorithmic paradigms used for ToA and multipath delay estimation. The survey in [15] serves as the main reference for algorithmic families in OFDM/CSI-based multiband sensing. From an OFDM-centric viewpoint, [18] also reviews multiband signal models and estimator families. Empirically, [19] compares representative super-resolution approaches for sub-7 GHz Wi-Fi multipath parameter estimation, illustrating practical differences under the bandwidth and antenna limitations of commodity devices.

Finally, a third direction develops resolution analysis and performance limits for multiband delay estimation, connecting spectral occupancy (aperture, band placement, and missing tones) to resolvability behavior through bounds and resolution metrics. For example, [20] uses CRLB-based criteria to select subbands under a LoS-plus-reflection model, emphasizing band selection for ranging rather than Wi-Fi channelization constraints. A more explicit treatment of how aperture and delay structure affect resolvability is provided via CRLB/SRL-based analyses in [18]. Complementarily, [21] extends the analysis beyond classical CRB/CRLB by capturing SNR-threshold effects and quantifying the impact of aperture, phase coherence, and impairments via tighter global bounds like the ones in the Zakai family.

While these works establish key principles for coherent splicing and multiband performance bounds, they typically consider abstract subband placements or emphasize calibration and band-design aspects rather than the Wi-Fi-regulated non-contiguous support induced by standardized channelization, spectral shaping, and omitted subcarriers. Related analysis discuss the aperture-sidelobe trade-off in the delay response [21], but do not explicitly connect spectral-gap geometry to sidelobe structure, spacing, and separation regimes that trigger multipath errors. In contrast, we specialize the analysis to standard-compliant Wi-Fi multiband configurations to directly quantify how gapped spectrum reshapes the delay-domain point-spread function, and we extend [10] with stronger bound-based grounding alongside an explicit delay-domain

characterization of gap-induced sidelobes.

B. Approaches for Multipath Delay Estimation

Performance limits are commonly studied through estimation-theoretic bounds, but their interpretation depends on the assumed estimation regime. Therefore, we briefly discuss two axes useful for interpreting bounds in noisy multipath channels with spectral gaps: (i) classical versus Bayesian formulations and (ii) unbiased versus biased estimation.

Classical formulations treat the delay of a multipath component τ as an unknown deterministic parameter. In this setting, the Cramér-Rao lower bound (CRLB) characterizes the best achievable variance among locally unbiased estimators using Fisher information [22], [23]. Bayesian formulations instead model τ as random with prior and target risk measures such as minimum mean-square error (MMSE), with the corresponding limits expressed through Bayesian bounds (e.g., Bayesian CRLB) [24].

Orthogonal to this distinction, an estimator $\hat{\tau}$ is unbiased if $\mathbb{E}[\hat{\tau} | \tau] = \tau$, whereas practical methods are often only approximately unbiased (e.g., asymptotically at high SNR) or deliberately biased through discretization, regularization, priors, or decision rules to reduce mean-square error (MSE), reflecting a bias-variance trade-off [22], [25].

In this work we primarily adopt the classical CRLB as a reference because it provides a clean, estimator-agnostic link between spectral occupancy and delay information through the Fisher information, thereby isolating the effect of non-contiguous support from algorithmic heuristics or priors. At the same time, CRLB is a local bound whose tightness relies on regularity conditions and a well-behaved (effectively unimodal) likelihood. Under gapped spectrum, the induced sidelobe structure can produce threshold behavior and outlier errors that are not captured by a purely local bound. For this reason, our analysis explicitly characterizes the gap-induced delay-domain sidelobes and ambiguities alongside CRLB-based grounding.

III. ANALYSIS FRAMEWORK

This section introduces the signal and observation models used throughout the paper. A unified frequency-domain formulation is adopted to describe both single-band and multiband Wi-Fi sensing scenarios on a common global frequency grid, while explicitly accounting for standard-compliant spectral shaping and non-contiguous spectrum occupancy. This framework provides a consistent basis for the subsequent analysis of delay estimation performance, including both estimation-theoretic bounds and delay-domain behavior under gapped spectrum.

A. Channel Model

We model the channel impulse response (CIR) as a sum of L propagation paths:

$$h(t) = \sum_{\ell=1}^L \alpha_{\ell} \delta(t - \tau_{\ell}), \quad (1)$$

where $\alpha_{\ell} \in \mathbb{C}$ is the complex gain and $\tau_{\ell} \in \mathbb{R}_+$ is the delay of path ℓ . The corresponding CFR is

$$H(f) = \sum_{\ell=1}^L \alpha_{\ell} e^{-j2\pi f \tau_{\ell}}. \quad (2)$$

To describe both single-band and multiband measurements in a unified way, we construct a global frequency grid spanning the overall measurement aperture $[f_{\text{start}}, f_{\text{stop}}]$:

$$f[n] = f_{\text{start}} + n\Delta f, \quad n = 0, 1, \dots, N_f - 1, \quad (3)$$

where f_{start} and f_{stop} denote the grid endpoints, Δf is the frequency spacing, and N_f is the total number of subcarriers on the grid. The corresponding total aperture is:

$$B_{\text{tot}} = f_{\text{stop}} - f_{\text{start}} = (N_f - 1)\Delta f. \quad (4)$$

While the framework can be extended to accommodate band-dependent spacings, we adopt a common Δf across all bands.

A multiband scenario s activates one or more Wi-Fi channels within this global grid. Spectral occupancy is described through a scenario-dependent spectral mask $a_s[n]$ defined on the full grid, $n = 0, \dots, N_f - 1$. The mask jointly captures the activated channel(s), omitted subcarriers within each channel bandwidth, guard and null tones, as well as the standard-defined Wi-Fi spectral shaping [26], which is approximately flat in-band and decays in the band-edge roll-off. For subcarriers that are not used or suppressed, $a_s[n] = 0$.

In the multiband case, the spectral mask can be decomposed into contributions from the individual channels. For a two-channel aggregation, we write:

$$a_s[n] = a_{s,1}[n] + a_{s,2}[n], \quad (5)$$

where $a_{s,1}[n]$ and $a_{s,2}[n]$ denote the standard-compliant spectral masks of the lower and upper Wi-Fi channels, respectively. Each sub-mask includes the corresponding in-band tones, omitted guard and null subcarriers, and is zero outside its associated channel. The spectral gap between the channels is therefore represented implicitly by the region where both $a_{s,1}[n]$ and $a_{s,2}[n]$ are zero.

For notational convenience in subsequent derivations, we define the set of used subcarriers as:

$$\mathcal{K}_s = \{n \in \{0, \dots, N_f - 1\} : a_s[n] \neq 0\}. \quad (6)$$

The CFR observation on the global grid is modeled as:

$$Y_s[n] = a_s[n] H(f[n]) + W_s[n], \quad n = 0, 1, \dots, N_f - 1, \quad (7)$$

The stacking operator $[\cdot]_{n \in \mathcal{K}_s}$ follows increasing subcarrier index n , $W_s[n] \sim \mathcal{CN}(0, \sigma_s^2)$ is additive complex Gaussian noise assumed independent across n , and σ_s^2 denotes the noise variance. This formulation applies to both single-band and multiband scenarios; the difference is entirely captured by the structure of the mask $a_s[n]$.

The observations can be embedded into the frequency-domain vector:

$$\mathbf{Y}_s = [Y_s[0] \ Y_s[1] \ \dots \ Y_s[N_f - 1]]^T, \quad (8)$$

which contains contiguous nonzero regions in the single-band case and separated regions in the multiband case, with zeros in the spectral gaps and outside the occupied channels.

If needed, an N_f -point inverse DFT can be computed to obtain a discrete CIR estimate:

$$y_s[p] = \frac{1}{N_f} \sum_{n=0}^{N_f-1} Y_s[n] e^{j2\pi np/N_f}, \quad p = 0, 1, \dots, N_f - 1. \quad (9)$$

This induces a delay sampling interval $T_s = (N_f \Delta f)^{-1}$ and a discrete delay axis $t[p] = pT_s$ for $p = 0, \dots, N_f - 1$. Because the inverse DFT is periodic, the resulting delay-domain representation spans an unambiguous window of length $N_f T_s = 1/\Delta f$.

Given noisy multiband CFR/CSI measurements collected under scenario s , the goal of multipath delay estimation is to estimate the delays of the dominant components, i.e., the parameter vector $\boldsymbol{\tau} = [\tau_1, \dots, \tau_L]^T$, and, depending on the estimator, also the corresponding complex gains $\boldsymbol{\alpha} = [\alpha_1, \dots, \alpha_L]^T$. Estimates can be obtained by processing the frequency-domain observations directly, or indirectly by transforming the measurements to the delay domain via (9) and identifying the dominant components on the resulting delay axis.

To study how multiband spectral occupancy affects the ability to distinguish closely spaced multipath components, we adopt a two-path channel model:

$$H(f) = \alpha_1 e^{-j2\pi f \tau_1} + \alpha_2 e^{-j2\pi f \tau_2}, \quad (10)$$

and parameterize path proximity by the delay separation:

$$\Delta\tau = \tau_2 - \tau_1. \quad (11)$$

Although richer multipath models with $L > 2$ are possible, the two-path setting provides a transparent baseline for interpreting resolvability effects and is therefore used throughout the subsequent analysis.

To avoid an arbitrary overall scaling, we normalize the dominant path gain to $\alpha_1 = 1$. We interpret α_1 as the dominant component (typically the LoS or strongest arrival) and α_2 as a single specular multipath component (e.g., a reflection). For the second path, we use a representative complex gain $\alpha_2 = \rho e^{j\phi}$ with $\rho = 0.7$ and $\phi = \pi/3$, i.e., $\alpha_2 \approx 0.35 + 0.606j$, which gives $|\alpha_2| \approx 0.7$ (about -3 dB in power relative to α_1). This choice fixes a nominal relative strength and phase so that comparisons across spectrum configurations and delay separations are made under the same channel point. Alternative choices of (ρ, ϕ) generally change the numerical values but do not affect the underlying formulation.

B. Multiband Wi-Fi Scenarios

Multiband sensing scenarios are constructed by activating one or two Wi-Fi channels withing single or multiple bands. Each scenario s is fully specified by the set \mathcal{K}_s and the corresponding standard-compliant spectral shaping $a_s[n]$, which captures the in-band flat region and band-edge roll-off of practical Wi-Fi transmissions. To quantify the impact of total used bandwidth, frequency aperture, and spectral gaps

TABLE I
MULTIBAND SIMULATION SCENARIOS. GROUP A USES 160 MHz OF TOTAL USED CHANNEL BANDWIDTH; GROUP B USES 320 MHz.

ID	Occupied bands [GHz]	Aperture [MHz]	Gap [MHz]
A1	[5.17, 5.33]	160	0
A2*	[5.25, 5.33], [5.49, 5.57]	320	160
A3*	[5.49, 5.57], [5.97, 6.05]	560	400
B1	[5.97, 6.13], [6.13, 6.29]	320	0
B2*	[5.17, 5.33], [5.49, 5.65]	480	160
B3*	[5.49, 5.65], [5.97, 6.13]	640	320

Note: Scenarios marked with * also include a contiguous reference allocation spanning the same aperture without the gap: A2*: [5.25, 5.57], A3*: [5.49, 6.05], B2*: [5.17, 5.65], and B3*: [5.49, 6.13].

on multipath delay resolution, we consider six representative configurations summarized in Table I and used consistently in the following analysis. These scenarios are also shown in Fig. 2, which positions them within the European Wi-Fi channelization framework under ETSI regulations for the 5 GHz and lower-6 GHz Wi-Fi operating spectrum.

Scenarios in group A uses 160 MHz of total occupied channel bandwidth, while group B uses 320 MHz. Within each group, the same total bandwidth is placed either contiguously within one band or split across separated 5/6 GHz allocations, producing increasingly gapped spectrum. Scenarios marked with * additionally include a contiguous reference allocation spanning the same aperture but without the gap, isolating the effect of spectral fragmentation.

IV. CRAMÉR-RAO LOWER BOUND

A CRLB benchmark is provided for the multiband observations in Equation (8). The benchmark quantifies the best possible accuracy of locally unbiased delay estimators under the assumed additive white Gaussian noise. The evaluation uses the two path channel model in Equation (10), with separation $\Delta\tau$ defined in Equation (11).

A. CRLB Derivation

For scenario s with occupied-tone set \mathcal{K}_s , restricting the global-grid model in Equation (7) to \mathcal{K}_s yields the stacked observation:

$$\mathbf{y}_s = [Y_s[n]]_{n \in \mathcal{K}_s} \in \mathbb{C}^{N_s}, \quad N_s = |\mathcal{K}_s|, \quad (12)$$

From Equation (7), $Y_s[n]$ includes the additive noise term $W_s[n]$. The observation satisfies:

$$\mathbf{y}_s | \boldsymbol{\theta} \sim \mathcal{CN}(\boldsymbol{\mu}_s(\boldsymbol{\theta}), \sigma_s^2 \mathbf{I}_{N_s}), \quad (13)$$

where \mathbf{I}_{N_s} denotes the $N_s \times N_s$ identity matrix and σ_s^2 is the per-tone noise variance over the occupied tones in scenario s . Accordingly, the noise is modeled as zero-mean circularly symmetric complex Gaussian with covariance $\sigma_s^2 \mathbf{I}_{N_s}$, meaning it has the same variance on each occupied tone and is uncorrelated across tones. The corresponding mean can be written as:

$$\boldsymbol{\mu}_s(\boldsymbol{\theta}) = \mathbf{A}_s \mathbf{X}_s(\boldsymbol{\tau}) \boldsymbol{\alpha}, \quad (14)$$

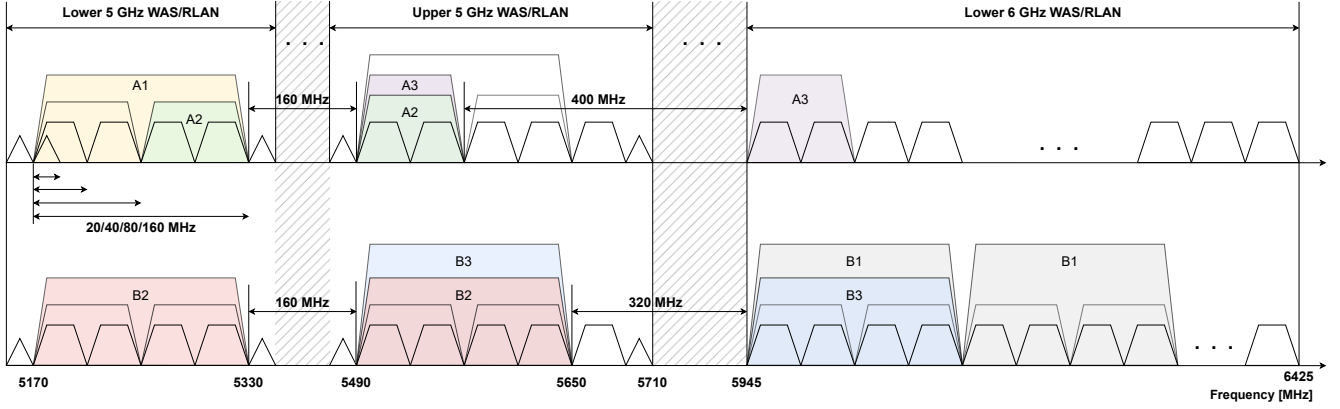


Fig. 2. Simulation scenarios A1-A3 and B1-B3 positioned within the European Wi-Fi channelization framework under ETSI regulations.

where:

$$\begin{aligned}
 \mathbf{A}_s &= \text{diag}([a_s[n]]_{n \in \mathcal{K}_s}), \\
 \boldsymbol{\tau} &= [\tau_1 \ \tau_2]^T, \\
 \boldsymbol{\alpha} &= [\alpha_1 \ \alpha_2]^T, \\
 \mathbf{X}_s(\boldsymbol{\tau}) &= [\mathbf{x}_s(\tau_1) \ \mathbf{x}_s(\tau_2)], \\
 \mathbf{x}_s(\tau_\ell) &= [e^{-j2\pi f[n]\tau_\ell}]_{n \in \mathcal{K}_s}.
 \end{aligned} \tag{15}$$

The parameter vector is:

$$\boldsymbol{\theta} = [\tau_1 \ \tau_2 \ \alpha_{1\text{Re}} \ \alpha_{1\text{Im}} \ \alpha_{2\text{Re}} \ \alpha_{2\text{Im}}]^T. \tag{16}$$

where $\alpha_\ell = \alpha_{\ell\text{Re}} + j\alpha_{\ell\text{Im}}$ for $\ell \in \{1, 2\}$. For each occupied subcarrier $n \in \mathcal{K}_s$ the corresponding entry of $\boldsymbol{\mu}_s(\boldsymbol{\theta})$ is:

$$\mu_s[n] = a_s[n] \sum_{\ell=1}^2 \alpha_\ell e^{-j2\pi f[n]\tau_\ell}, \quad n \in \mathcal{K}_s. \tag{17}$$

For the model in Equation (13), the Fisher information matrix (FIM) entries follow the standard complex Gaussian form [20], [22]:

$$[\mathbf{I}_s(\boldsymbol{\theta})]_{ij} = \frac{2}{\sigma_s^2} \Re \left\{ \frac{\partial \boldsymbol{\mu}_s^H}{\partial \theta_i} \frac{\partial \boldsymbol{\mu}_s}{\partial \theta_j} \right\}, \quad i, j \in \{1, 2, 3, 4, 5, 6\}. \tag{18}$$

Defining $\mathbf{d}_i = \partial \boldsymbol{\mu}_s / \partial \theta_i$, Equation (18) can be written equivalently as $[\mathbf{I}_s(\boldsymbol{\theta})]_{ij} = \frac{2}{\sigma_s^2} \Re \{ \mathbf{d}_i^H \mathbf{d}_j \}$. Derivative vectors and closed form FIM entries are listed in Appendix A.

To isolate the information about $\boldsymbol{\tau}$, the FIM in Equation (18) can also be partitioned according to the parameter ordering $\boldsymbol{\theta} = [\boldsymbol{\tau}^T \ \boldsymbol{\alpha}_R^T]^T$, where $\boldsymbol{\alpha}_R = [\alpha_{1\text{Re}} \ \alpha_{1\text{Im}} \ \alpha_{2\text{Re}} \ \alpha_{2\text{Im}}]^T$, yielding the blocks $\mathbf{I}_{\tau\tau}$, $\mathbf{I}_{\tau\alpha}$, $\mathbf{I}_{\alpha\tau}$, and $\mathbf{I}_{\alpha\alpha}$.

Then, the effective information for $\boldsymbol{\tau}$ is the Schur complement:

$$\mathbf{I}_{\text{eff}}(\boldsymbol{\tau}) = \mathbf{I}_{\tau\tau} - \mathbf{I}_{\tau\alpha} \mathbf{I}_{\alpha\alpha}^{-1} \mathbf{I}_{\alpha\tau}, \tag{19}$$

The CRLB for any locally unbiased $\hat{\boldsymbol{\tau}}$ now is:

$$\text{cov}(\hat{\boldsymbol{\tau}}) \succeq \mathbf{I}_{\text{eff}}^{-1}(\boldsymbol{\tau}). \tag{20}$$

For the separation $\Delta\tau = \tau_2 - \tau_1$ from Equation (11), we can write $\Delta\tau = \mathbf{g}^T \boldsymbol{\tau}$ with $\mathbf{g} = [-1 \ 1]^T$. The corresponding CRLB then is:

$$\text{var}(\widehat{\Delta\tau}) \geq \mathbf{g}^T \mathbf{I}_{\text{eff}}^{-1}(\boldsymbol{\tau}) \mathbf{g}. \tag{21}$$

B. CRLB Results

Delay separation resolvability is quantified using the CRLB for the parameter $\Delta\tau = \tau_2 - \tau_1$, obtained from the effective FIM. Square-root CRLB represents a lower bound on the standard deviation of any unbiased estimator of the delay separation. Smaller values indicate improved local resolvability of closely spaced multipath components, while larger values correspond to increased estimation uncertainty. All CRLB results are evaluated for the two-path channel model in Section III-A, with the dominant path normalized to $\alpha_1 = 1$ and the second path parameterized as $\alpha_2 = \rho e^{j\phi}$ with $\rho = 0.7$ and $\phi = \pi/3$.

We define SNR as the average per occupied-tone (noiseless) power-to-noise ratio:

$$\text{SNR} = \frac{\|\boldsymbol{\mu}_s(\boldsymbol{\theta})\|_2^2 / N_s}{\sigma_s^2} = \frac{1}{N_s} \sum_{n \in \mathcal{K}_s} \frac{|\mu_s[n]|^2}{\sigma_s^2}, \tag{22}$$

where $N_s = |\mathcal{K}_s|$ and $\boldsymbol{\mu}_s(\boldsymbol{\theta})$ is given in Equations (14) and (17). For a target SNR_{dB} , we set:

$$\sigma_s^2 = (\|\boldsymbol{\mu}_s(\boldsymbol{\theta}_0)\|_2^2 / N_s) / 10^{\text{SNR}_{\text{dB}}/10}, \tag{23}$$

where $\boldsymbol{\theta}_0$ denotes the parameter point used to evaluate the bound. Since the noise variance is common across occupied tones, allocation-dependent CRLB differences arise from how the allocation changes the mean model and the observed subcarrier set via $a_s[n]$ and $f[n]$, rather than from unequal per-tone measurement reliability.

Figure 3 shows $\sqrt{\text{CRLB}(\Delta\tau)}$ versus SNR for scenario groups A and B at two representative separations, $\Delta\tau \in \{1 \text{ ns}, 10 \text{ ns}\}$. These correspond to excess path lengths $\Delta d = c\Delta\tau$, so $\Delta\tau = 1 \text{ ns}$ maps to $\Delta d \approx 0.30 \text{ m}$ and $\Delta\tau = 10 \text{ ns}$ maps to $\Delta d \approx 3 \text{ m}$, which is realistic for indoor environments.

We first compare, within each group, cases with the same occupied bandwidth: the contiguous baseline (A1/B1) and the gapped allocations (A2-A3/B2-B3), which use the same number of subcarriers but span a larger aperture. Across both separations, the gapped allocations achieve lower bounds, indicating that the dominant effect is the increased effective

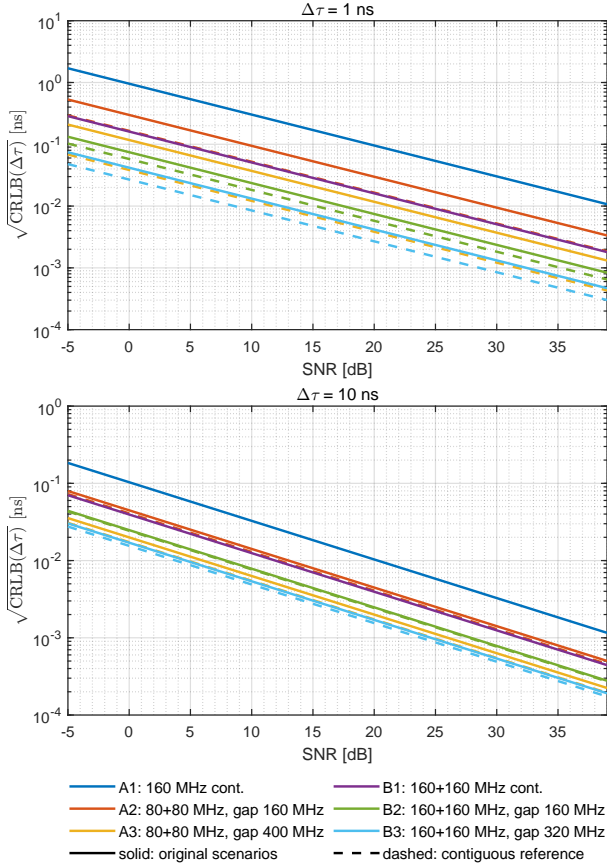


Fig. 3. Square-root CRLB of $\Delta\tau$ versus SNR for scenarios A1-A3 and B1-B3, shown for $\Delta\tau = 1$ ns (top) and $\Delta\tau = 10$ ns (bottom), with $\alpha_1 = 1$ and $\alpha_2 = 0.7e^{j\pi/3}$. Contiguous references are included for the gapped cases.

frequency aperture. Across both separations, the gapped allocations achieve lower bounds, indicating that the dominant effect is the increased effective frequency aperture. This follows directly from the delay-delay block of the FIM: the diagonal terms I_{11} and I_{22} scale with the quadratic frequency sum $\sum_{n \in \mathcal{K}_s} |a_s[n]|^2 f[n]^2$, and this scaling carries into the effective delay information \mathbf{I}_{eff} and enters the corresponding CRLB in (21).

To quantify fragmentation effects, each gapped allocation (solid) is also compared to a hypothetical contiguous reference (dashed) defined over the same overall aperture. This reference assumes an OFDM tone grid with the standard subcarrier spacing $\Delta f = 78.125$ kHz spanning the full aperture. Relative to this reference, the gapped allocations exhibit a slightly higher bound, with the gap-induced penalty being more pronounced at $\Delta\tau = 1$ ns than at $\Delta\tau = 10$ ns. This separation dependence motivates the $\Delta\tau$ sweep in Fig. 4.

Figure 4 shows $\sqrt{\text{CRLB}(\Delta\tau)}$ as a function of $\Delta\tau$ at SNR = 20 dB. The advantage of a larger frequency aperture is evident from the lower overall bound levels achieved by the allocations with bigger aperture. However, comparing each gapped allocation (solid) with its hypothetical contiguous reference over the same aperture (dashed) isolates the effect of the internal gap. For separations smaller than 1 ns, the gapped curves exhibit an approximately constant gap-induced penalty relative to the corresponding contiguous (dashed)

reference. At larger separations, the gapped scenarios first develop pronounced oscillations and, for sufficiently large $\Delta\tau$, i.e. separations bigger than 10 ns, approach nearly the same square-root CRLB levels as the aperture-matched contiguous reference (dashed).

The separation-selective oscillations in Fig. 4 originate from the separation-dependent cross-path coupling terms in the FIM, which involve coherent sums across the occupied tones. For example, the delay-delay coupling entry I_{12} in (36) contains the term:

$$\sum_{n \in \mathcal{K}_s} |a_s[n]|^2 f[n]^2 e^{-j2\pi f[n]\Delta\tau}, \quad (24)$$

so that as $\Delta\tau$ varies, the phasor factor $e^{-j2\pi f[n]\Delta\tau}$ rotates across frequency and changes the degree of constructive/destructive addition in this sum. This modulates the effective coupling between the two delays and, through the Schur-complement reduction used to form \mathbf{I}_{eff} , produces peaks and dips in $\text{CRLB}(\Delta\tau)$.

For two-subband (gapped) allocations, the characteristic oscillation scale is set primarily by the center-to-center spacing between the occupied subbands:

$$\Delta f_c = f_{c,2} - f_{c,1}, \quad (25)$$

with $f_{c,1}$ and $f_{c,2}$ denoting the subband center frequencies. Consistent with [21], prominent extrema occur at separations on the order of $\Delta\tau \approx n/\Delta f_c$. In our scenarios, $\Delta f_c \in \{240, 480, 320, 480\}$ MHz for A2, A3, B2, and B3, respectively, and corresponding characteristic spacings $1/\Delta f_c \approx \{4.2, 2.1, 3.1, 2.1\}$ ns around which we see pronounced oscillations. Accordingly, the larger-gap configurations exhibit stronger and denser oscillations, with A3 showing the most pronounced ripple.

The detailed shape of the oscillations differs from the idealized setting in [21] because of Wi-Fi-like spectral masks, guard structure, and nonuniform subcarrier weights inside each channel mask that reduce perfect coherence and therefore broaden and soften the extrema. In addition, the oscillation amplitude and phase depend on the relative magnitude and phase of α_2/α_1 , since this ratio enters the cross-path FIM terms: not only through I_{12} , but also through the separation-dependent delay-gain mixed entries (e.g., I_{15} , I_{16} , I_{23} , and I_{24}), which contain α_1 or α_2 multiplying coherent sums of the form $\sum_{n \in \mathcal{K}_s} |a_s[n]|^2 f[n] e^{\pm j2\pi f[n]\Delta\tau}$ and therefore further shape \mathbf{I}_{eff} via the Schur complement. While varying α_2/α_1 shifts the absolute bound level and reshapes the oscillations pattern, the overall trends persist. Increasing frequency aperture improves the bound on average, whereas spectral fragmentation increases separation-selective variability.

Finally, we emphasize that the CRLB is a local bound. It is determined by the FIM at the true parameter and therefore captures local sensitivity and inter-parameter coupling (including inter-path coupling in the two-path model). However, it characterizes performance only within the correct likelihood basin and does not account for global failures such as selecting an incorrect delay peak. The delay-response analysis in Section V therefore complements the CRLB results by linking gap geometry to sidelobe structure and identifying regimes in

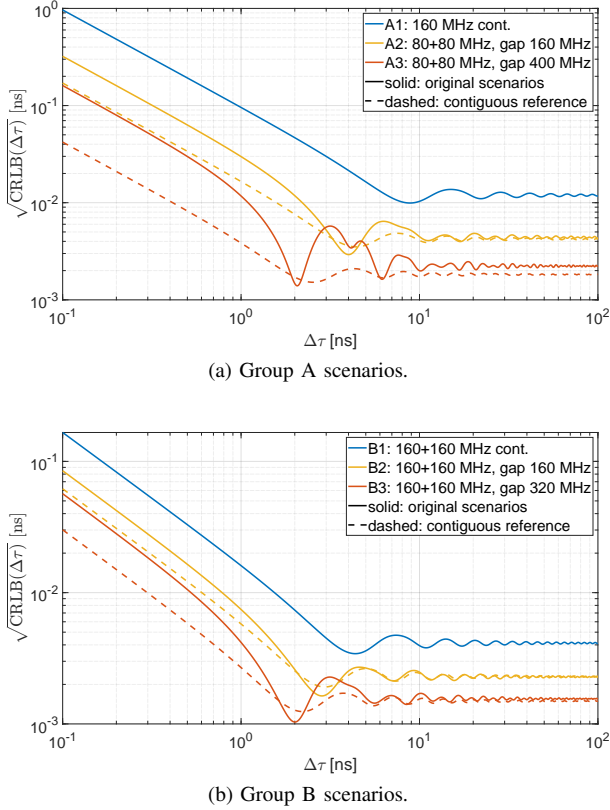


Fig. 4. Square-root CRLB of $\Delta\tau$ versus $\Delta\tau$ (ns) at SNR = 20 dB, with $\alpha_1 = 1$ and $\alpha_2 = 0.7e^{j\pi/3}$. Contiguous references are included for the gapped cases.

which peak ambiguities, rather than local variance, dominate practical estimation performance.

V. GAP-INDUCED SIDELOBES

Non-contiguous allocations reshape the delay-domain behavior beyond what is captured by the CRLB alone. The CRLB provides a local variance bound under the assumed model, effectively describing performance within the correct likelihood basin. However, under gapped spectrum, the occupied tones and their standard-defined weights act as an effective spectral window whose delay-domain response exhibits deterministic sidelobes. These gap-induced sidelobes can produce competing peaks and separation-selective ambiguities, so practical estimators that rely on correlation or peak picking may exhibit outliers and threshold effects even when the CRLB remains small. This section therefore characterizes the sidelobe structure induced by gaps and then connects sidelobe metrics to the observed regimes where CRLB trends do and do not reflect practical performance.

A. Delay Response and Sidelobes: Single Path Case

Many ToA and multipath delay estimators operate by testing candidate delays τ and evaluating how well the measured CFR matches the corresponding delay-dependent phase progression on the available tones. Under (7), scenario s provides CFR samples only on the subcarrier index set \mathcal{K}_s ; those samples are deterministically shaped by the known multiband mask $a_s[n]$,

where $n \in \mathcal{K}_s$ and $f[n]$ denotes the absolute frequency of tone n . The occupied subcarriers and their weights, therefore act as an effective spectral window whose delay-domain response governs the deterministic sidelobe pattern of any correlation-based delay test.

To illustrate this effect, we consider the noise-free single-path case of (2), $H(f) = \alpha e^{-j2\pi f\tau_0}$, where τ_0 is the true path delay and α is its complex gain. Correlating the noise-free observed CFR with a candidate single-path signature $a_s[n]e^{-j2\pi f[n]\tau}$ yields:

$$g_s(\tau - \tau_0) = \sum_{n \in \mathcal{K}_s} |a_s[n]|^2 e^{-j2\pi f[n](\tau - \tau_0)}. \quad (26)$$

The factor $|a_s[n]|^2$ arises because the correlation uses the conjugate mask, so (26) is the discrete Fourier transform of the effective spectral window over the occupied subcarriers. The magnitude is normalized as $|g_s(\tau)|/|g_s(0)|$, so that the response attains unity at the true delay $\tau = \tau_0$. With a unit-amplitude path placed at $\tau_0 = 0$, $|g_s(\tau)|/|g_s(0)|$ gives the normalized single-path delay response versus tested delay τ ; values away from $\tau = 0$ directly quantify the deterministic sidelobe level (leakage) induced by the subcarrier set \mathcal{K}_s and the mask weights $a_s[n]$.

Figure 5 shows the normalized magnitude of the single-path delay response $|g_s(\tau)|$ for the allocations in Groups A and B. Solid curves correspond to the original allocations, while dashed curves show the contiguous reference variants for the gapped cases. In both groups, contiguous allocations produce a single dominant mainlobe followed by smoothly decaying sidelobes. Comparing each gapped allocation to its contiguous reference shows that the internal gap introduces oscillations superimposed on an overall decay that closely follows the span-matched contiguous case; the gap also shifts the locations of both the local maximas and minimas.

To explain the oscillatory sidelobe structure induced by spectral gaps, it is convenient to rewrite $g_s(\tau)$ as the coherent sum of the two occupied subbands. Using the lower- and upper-subband index sets $\mathcal{K}_{s,1}$ and $\mathcal{K}_{s,2}$ and their center frequencies $f_{c,1}$ and $f_{c,2}$, we decompose the multiband mask $a_s[n]$ into its subband-supported components $a_{s,1}[n]$ and $a_{s,2}[n]$. Since the single-path correlation response in (26) weights each occupied tone by the mask power, we use $|a_{s,i}[n]|^2$ as the per-tone weights within subband i , normalized by the total mask power which yields $g_s(0) = 1$.

To factor out the subband-center phase term and isolate the within-subband shape, we define the basebanded response of each subband $i \in \{1, 2\}$ as:

$$G_i(\tau) = \sum_{n \in \mathcal{K}_{s,i}} \frac{|a_{s,i}[n]|^2}{\sum_{m \in \mathcal{K}_s} |a_s[m]|^2} e^{-j2\pi(f[n] - f_{c,i})\tau}. \quad (27)$$

Then the overall response can be written as

$$g_s(\tau) = e^{-j2\pi f_{c,1}\tau} G_1(\tau) + e^{-j2\pi f_{c,2}\tau} G_2(\tau). \quad (28)$$

Equation (28) directly yields the two-scale behavior observed for gapped allocations. The slowly varying envelope is governed by the magnitudes $|G_1(\tau)|$ and $|G_2(\tau)|$,

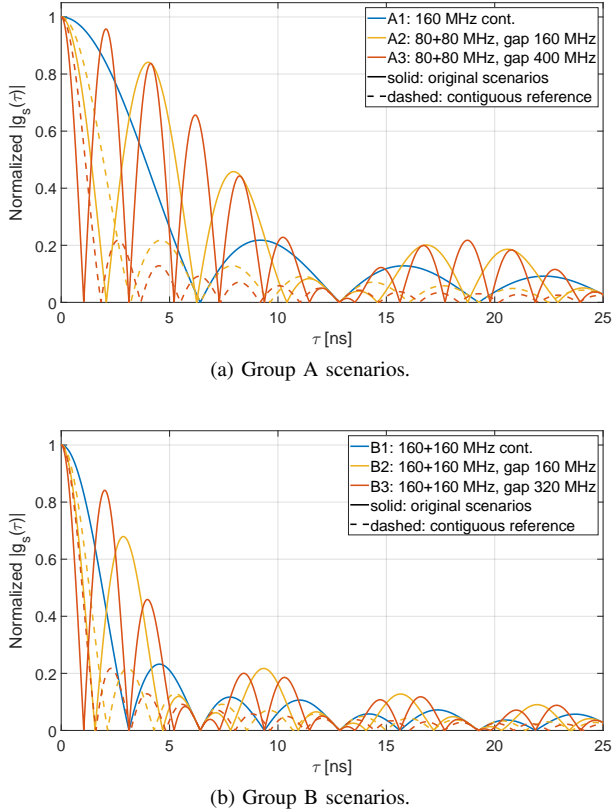


Fig. 5. Normalized single-path delay response $|g_s(\tau)|$ defined in (26) for Groups A and B.

which are set primarily by the contiguous subband bandwidth B_{sb} and the within-subband weighting. When the two subbands have comparable structure (e.g., similar bandwidth and weighting), these envelopes are similar and define a common decay profile. Superimposed on this envelope is a faster oscillatory modulation arising from the relative phase rotation between the two subband contributions. Specifically, the phase difference evolves as $2\pi\Delta f_c \tau$, producing alternating reinforcement and cancellation with characteristic spacing on the order of $1/\Delta f_c$. In the symmetric case, deep minima occur near $\tau \approx (m + \frac{1}{2})/\Delta f_c$, $m = 0, 1, 2, \dots$, where the two subband contributions are approximately out of phase. Additional near-zeros can occur due to the intrinsic null structure of $G_i(\tau)$ itself; thus, the observed minima reflect the combined effect of the per-subband envelope (set by B_{sb} and weighting) and inter-subband interference (set by Δf_c). For illustration, consider scenario A2, for which $\Delta f_c = 240$ MHz and $B_{sb} = 80$ MHz. This yields gap-induced minima near $\tau_{0,m} \approx \{2.08, 6.25, 10.42, 14.58, 18.75, \dots\}$ ns. In addition, the main envelope produces minima at roughly integer multiples of $1/B_{sb}$, which for A2 corresponds to $\{12.5, 25, \dots\}$ ns.

B. Delay Response and Sidelobes: Two Paths Case

The single-path response $g_s(\tau)$ captures how a gapped spectral window maps into deterministic delay sidelobes. In practice, we have multipath environment and the received CFR is a superposition of multiple delay-dependent phase progressions that belong to those multipath components, so

the same sidelobe structure directly affects practical estimators that scan candidate delays and select peaks.

To illustrate this, we consider a two-path model from (10). Then, a standard matched-filter delay scan is obtained by testing candidate delays τ . For each τ , the measured CFR samples on the occupied tones are correlated with the phase progression that a single propagation path at delay τ would induce across frequency, i.e., $e^{-j2\pi f[n]\tau}$, using the same mask-based weighting as in (26). For scenario s , the resulting noise-free scan is:

$$T_s(\tau) = \left| \sum_{n \in \mathcal{K}_s} |a_s[n]|^2 H(f[n]) e^{j2\pi f[n]\tau} \right| \quad (29)$$

$$= |\alpha_1 g_s(\tau - \tau_1) + \alpha_2 g_s(\tau - \tau_2)|.$$

The scan is the magnitude of a superposition of two shifted copies of the single-path response. Unlike $|g_s(\tau)|$, the $T_s(\tau)$ is not normalized later and its magnitude is scenario-dependent. It scales with α_1, α_2 as well as with the coherent superposition of the two contributions $\alpha_1 g_s(\tau - \tau_1)$ and $\alpha_2 g_s(\tau - \tau_2)$.

Fig. 6 visualizes the two-path scan response $T_s(\tau)$ under presented scenarios, highlighting how sidelobe structure and peak contrast change with spectral gaps. SNR is set to 20 dB, with $\alpha_1 = 1$ and $\alpha_2 = 0.7e^{j\pi/3}$. The two delays are selected above the nominal span-limited resolvability of the smallest contiguous baselines, while remaining in a regime where sidelobe interactions can be visually assessed. Specifically, Group A uses $(\tau_1, \tau_2) = (5, 15)$ ns, and Group B uses $(\tau_1, \tau_2) = (5, 10)$ ns. These values are chosen so that path separations exceed the $1/BW$ resolution limit of contiguous baseline scenarios A1 and B1 (approximately 6.25 ns and 3.13 ns respectively). This highlights how introducing a spectral gap, while using the same total bandwidth, just with the gap inbetween and increased aperture changes the effective delay response, most notably the sidelobe structure and the contrast between the two peaks, relative to single-band baseline.

Table II quantifies the peak distortions visible in Fig. 6. The estimate $\hat{\tau}_i$ is location of the largest value of $|T_s(\tau)|$ obtained by restricted search over a small neighborhood around true delay τ_i . The results show that a larger aperture can sharpen the mainlobe (e.g., A3 versus A1), but that gap-shaped sidelobes and the relative path configuration can still pull the peak away from the true delay, even when the mainlobe is sharper (e.g., A2 versus A1 for second path). Consequently, increasing aperture does not translate monotonically into improved multipath localization. Performance is jointly governed by mainlobe sharpness and the sidelobe/ambiguity structure induced by the allocation and the specific multipath geometry.

C. Sidelobe Leakage and Practical Impact

Taking into account the delay-response behavior under non-contiguous spectrum, the CRLB is complemented with an explicit sidelobe/leakage characterization. The CRLB predicts local estimation variance within the correct likelihood basin, whereas deterministic sidelobes can introduce ambiguity and separation-dependent coupling between paths that is not reflected in the bound. This motivates introducing a normalized leakage function to interpret the two-path CRLB curve.

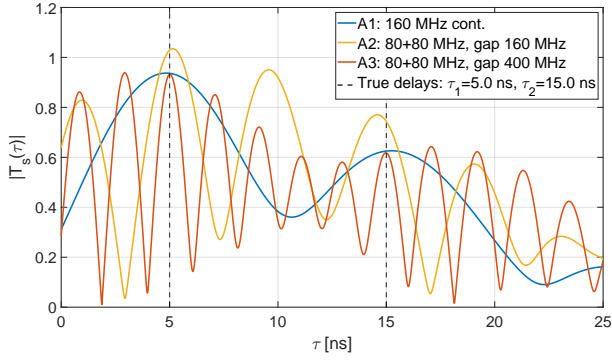
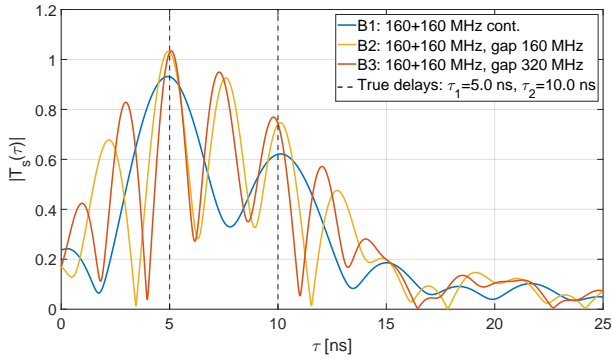
(a) Group A scenarios ($\tau_1 = 5$ ns, $\tau_2 = 15$ ns).(b) Group B scenarios ($\tau_1 = 5$ ns, $\tau_2 = 10$ ns).Fig. 6. Two-path matched-filter delay scans $T_s(\tau)$ at SNR = 20 dB, with $\alpha_1 = 1$ and $\alpha_2 = 0.7e^{j\pi/3}$. Vertical dashed lines mark the true delays.

TABLE II

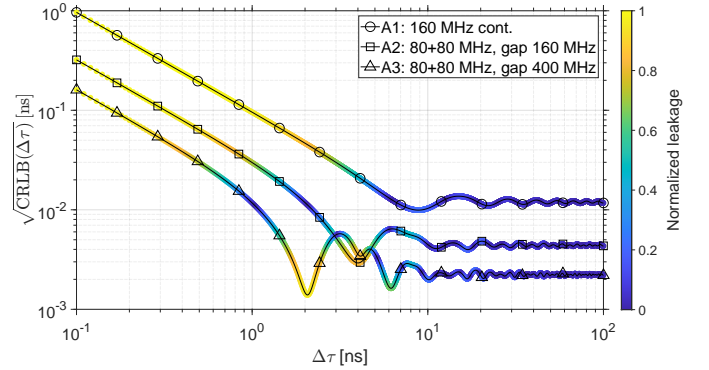
LOCAL PEAK LOCATIONS OF THE TWO-PATH MATCHED-FILTER SCAN $|T_s(\tau)|$ IN A NEIGHBORHOOD OF EACH TRUE DELAY. REPORTED ARE THE ESTIMATED PEAK POSITIONS $\hat{\tau}_l$ AND THE OFFSETS $\Delta\tau_l = \hat{\tau}_l - \tau_l$.

ID	$\hat{\tau}_1$ [ns]	$\Delta\tau_1$ [ns]	$\hat{\tau}_2$ [ns]	$\Delta\tau_2$ [ns]
A1	4.839	-0.161	15.229	+0.229
A2	5.156	+0.156	14.591	-0.409
A3	5.019	+0.019	14.975	-0.025
B1	4.916	-0.084	10.116	+0.116
B2	4.943	-0.057	10.108	+0.108
B3	5.080	+0.080	9.792	-0.208

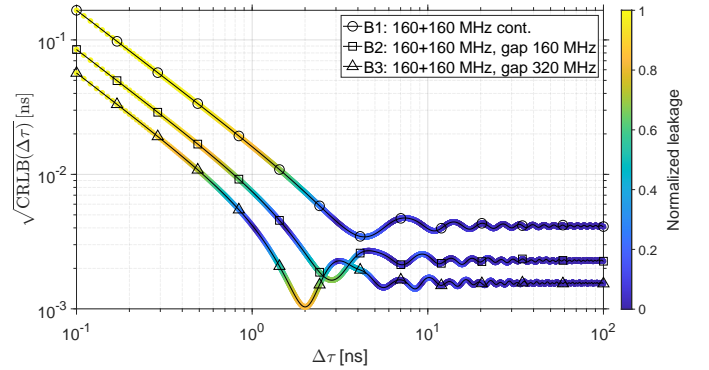
To connect the CRLB trends to the sidelobe structure, we annotate the two-path CRLB curve $\sqrt{\text{CRLB}(\Delta\tau)}$, computed from (21) using a normalized leakage level derived from the single-path response in (26). For scenario s , we evaluate:

$$\ell_s(\Delta\tau) = \frac{|g_s(\Delta\tau)|}{|g_s(0)|}, \quad (30)$$

where $\Delta\tau$ is the relative delay defined in (11). This quantity is the normalized magnitude of the correlation response at an offset $\Delta\tau$, and it directly measures how much a unit path at one delay leaks into a hypothesis offset by $\Delta\tau$ under the same tone set \mathcal{K}_s and weights $|a_s[n]|^2$. In the two-path scan in (29), this leakage appears symmetrically in both directions, so evaluating the scan at $\tau = \tau_1$ contains an undesired contribution proportional to $\alpha_2 g_s(\tau_1 - \tau_2)$, while evaluating it at $\tau = \tau_2$ contains an undesired contribution proportional to



(a) Group A scenarios.



(b) Group B scenarios.

Fig. 7. $\sqrt{\text{CRLB}(\Delta\tau)}$ versus $\Delta\tau$, with color indicating the normalized leakage level $\ell_s(\Delta\tau)$ at SNR = 20 dB, with $\alpha_1 = 1$ and $\alpha_2 = 0.7e^{j\pi/3}$.

$\alpha_1 g_s(\tau_2 - \tau_1)$. In radar literature, related sidelobe summaries are often reported as a single scalar, e.g., peak sidelobe level as $\max_{\tau \neq 0} |g_s(\tau)|/|g_s(0)|$, or integrated sidelobe level as an energy-type integral over $\tau \neq 0$. Here we keep the full separation-dependent function $\ell_s(\Delta\tau)$ because the relevant coupling between two paths depends on the actual separation $\Delta\tau$.

Figure 7 shows $\sqrt{\text{CRLB}(\Delta\tau)}$ with color indicating the separation-dependent leakage level $\ell_s(\Delta\tau)$. The key observation is that non-contiguous allocations produce an oscillatory leakage pattern, consistent with the sidelobes in Fig. 5. These oscillations explain the non-monotone behavior of the CRLB versus $\Delta\tau$: separations where $\ell_s(\Delta\tau)$ is small (blue) correspond to weaker inter-path coupling and typically lower $\sqrt{\text{CRLB}(\Delta\tau)}$, whereas separations where $\ell_s(\Delta\tau)$ is larger (yellow/green) indicate stronger coupling and a degraded bound and performance. Relative to contiguous baselines, gapped allocations therefore exhibit separation-selective identifiability: some separations benefit from leakage nulls, while others remain difficult due to leakage peaks, even at the same total span. Importantly, the high-leakage regions are also where practical delay scans in (29) are most prone to peak competition and peak pulling, so estimators can exhibit outliers in regimes that a purely local CRLB does not capture.

VI. CONCLUSION

This paper investigates multipath delay estimation under Wi-Fi compliant non-contiguous spectrum by combining estimation-theoretic analysis with an explicit characterization of gap-induced delay domain behavior. The results show that, while multiband aggregation is fundamentally beneficial due to increased frequency aperture, spectral fragmentation introduces structured effects that strongly influence practical resolvability.

The CRLB analysis confirms that the larger effective apertures generally reduce the achievable variance of delay separation estimates, even when the spectrum is split across distant subbands. This supports the use of multiband aggregation in Wi-Fi based ISAC systems. However, gapped allocations exhibit pronounced separation-dependent oscillations in the bound, caused by inter-path coupling across disjoint frequency regions. Consequently, delay resolvability depends not only on total aperture of occupied bandwidth, but also on the placement and geometry of spectral gaps.

Beyond the CRLB bound, delay-domain analysis shows that non-contiguous spectrum fundamentally reshapes the delay response through deterministic sidelobes, whose spacing is determined primarily by the separation between subband centers and persist even at high SNR. As a result, practical delay estimators based on correlation or peak selection may experience competing peaks or outliers in regimes where CRLB remains small, highlighting the limitations of local performance interpretation. The proposed normalized leakage metric provides a direct link between spectral occupancy and these effects. By quantifying separation-dependent coupling induced by the gapped spectral window, the metric explains both the oscillatory behavior of the CRLB and the ambiguous peaks in practical delay scans. Compared to contiguous allocations, gapped configurations exhibit a structured sidelobes in which some path separations become easier to resolve, while others remain prone to strong coupling despite identical total bandwidth of used channels.

These observations point to several promising research directions. While the CRLB characterizes local performance limits, non-contiguous spectrum requires global and ambiguity-aware performance metrics. Moreover, gap-aware estimation methods should include sidelobe-weighting and multi-peak testing to exploit favorable leakage conditions or avoid highly ambiguous scenarios and further enhance robustness in Wi-Fi sensing.

APPENDIX

A. FIM Structure and Index Mapping

For $\boldsymbol{\theta} = [\tau_1 \ \tau_2 \ \alpha_{1\text{Re}} \ \alpha_{1\text{Im}} \ \alpha_{2\text{Re}} \ \alpha_{2\text{Im}}]^T$, the 6×6 FIM can be written as:

$$\mathbf{I}_s(\boldsymbol{\theta}) = \begin{bmatrix} I_{11} & I_{12} & I_{13} & I_{14} & I_{15} & I_{16} \\ I_{21} & I_{22} & I_{23} & I_{24} & I_{25} & I_{26} \\ I_{31} & I_{32} & I_{33} & I_{34} & I_{35} & I_{36} \\ I_{41} & I_{42} & I_{43} & I_{44} & I_{45} & I_{46} \\ I_{51} & I_{52} & I_{53} & I_{54} & I_{55} & I_{56} \\ I_{61} & I_{62} & I_{63} & I_{64} & I_{65} & I_{66} \end{bmatrix} = \begin{bmatrix} \mathbf{I}_{\tau\tau} & \mathbf{I}_{\tau\alpha} \\ \mathbf{I}_{\alpha\tau} & \mathbf{I}_{\alpha\alpha} \end{bmatrix}, \quad (31)$$

with:

$$I_{ij} = \frac{2}{\sigma_s^2} \Re\{\mathbf{d}_i^H \mathbf{d}_j\}, \quad (32)$$

and the index order:

$$(1, 2, 3, 4, 5, 6) \leftrightarrow (\tau_1, \tau_2, \alpha_{1\text{Re}}, \alpha_{1\text{Im}}, \alpha_{2\text{Re}}, \alpha_{2\text{Im}}). \quad (33)$$

B. Derivative Vectors

The derivative vectors are:

$$\begin{aligned} \mathbf{d}_1 &= \frac{\partial \boldsymbol{\mu}_s}{\partial \tau_1} = -j2\pi\alpha_1 [a_s[n] f[n] e^{-j2\pi f[n]\tau_1}]_{n \in K_s} \\ \mathbf{d}_2 &= \frac{\partial \boldsymbol{\mu}_s}{\partial \tau_2} = -j2\pi\alpha_2 [a_s[n] f[n] e^{-j2\pi f[n]\tau_2}]_{n \in K_s} \\ \mathbf{d}_3 &= \frac{\partial \boldsymbol{\mu}_s}{\partial \alpha_{1\text{Re}}} = [a_s[n] e^{-j2\pi f[n]\tau_1}]_{n \in K_s} \\ \mathbf{d}_4 &= \frac{\partial \boldsymbol{\mu}_s}{\partial \alpha_{1\text{Im}}} = j[a_s[n] e^{-j2\pi f[n]\tau_1}]_{n \in K_s} \\ \mathbf{d}_5 &= \frac{\partial \boldsymbol{\mu}_s}{\partial \alpha_{2\text{Re}}} = [a_s[n] e^{-j2\pi f[n]\tau_2}]_{n \in K_s} \\ \mathbf{d}_6 &= \frac{\partial \boldsymbol{\mu}_s}{\partial \alpha_{2\text{Im}}} = j[a_s[n] e^{-j2\pi f[n]\tau_2}]_{n \in K_s} \end{aligned} \quad (34)$$

Here $\alpha_1 = \alpha_{1\text{Re}} + j\alpha_{1\text{Im}}$ and $\alpha_2 = \alpha_{2\text{Re}} + j\alpha_{2\text{Im}}$.

C. Delay-Delay Block

The diagonal delay terms are:

$$\begin{aligned} I_{11} &= \frac{2}{\sigma_s^2} \Re\{\mathbf{d}_1^H \mathbf{d}_1\} = \\ &= \frac{8\pi^2}{\sigma_s^2} (\alpha_{1\text{Re}}^2 + \alpha_{1\text{Im}}^2) \sum_{n \in K_s} |a_s[n]|^2 f[n]^2, \\ I_{22} &= \frac{2}{\sigma_s^2} \Re\{\mathbf{d}_2^H \mathbf{d}_2\} = \\ &= \frac{8\pi^2}{\sigma_s^2} (\alpha_{2\text{Re}}^2 + \alpha_{2\text{Im}}^2) \sum_{n \in K_s} |a_s[n]|^2 f[n]^2. \end{aligned} \quad (35)$$

The off-diagonal delay terms are:

$$\begin{aligned} I_{12} = I_{21} &= \frac{8\pi^2}{\sigma_s^2} \Re\left\{ (\alpha_{2\text{Re}} + j\alpha_{2\text{Im}})(\alpha_{1\text{Re}} - j\alpha_{1\text{Im}}) \right. \\ &\quad \left. \times \sum_{n \in K_s} |a_s[n]|^2 f[n]^2 e^{-j2\pi f[n](\tau_2 - \tau_1)} \right\}. \end{aligned} \quad (36)$$

D. Gain-Gain Block

The gain-related terms are:

$$\begin{aligned} I_{33} &= \frac{2}{\sigma_s^2} \Re\{\mathbf{d}_3^H \mathbf{d}_3\} = \frac{2}{\sigma_s^2} \sum_{n \in K_s} |a_s[n]|^2, \\ I_{44} &= \frac{2}{\sigma_s^2} \Re\{\mathbf{d}_4^H \mathbf{d}_4\} = \frac{2}{\sigma_s^2} \sum_{n \in K_s} |a_s[n]|^2, \\ I_{55} &= \frac{2}{\sigma_s^2} \Re\{\mathbf{d}_5^H \mathbf{d}_5\} = \frac{2}{\sigma_s^2} \sum_{n \in K_s} |a_s[n]|^2, \\ I_{66} &= \frac{2}{\sigma_s^2} \Re\{\mathbf{d}_6^H \mathbf{d}_6\} = \frac{2}{\sigma_s^2} \sum_{n \in K_s} |a_s[n]|^2. \end{aligned} \quad (37)$$

The within-path gain cross terms are:

$$\begin{aligned} I_{34} = I_{43} &= \frac{2}{\sigma_s^2} \Re\{\mathbf{d}_3^H \mathbf{d}_4\} = 0, \\ I_{56} = I_{65} &= \frac{2}{\sigma_s^2} \Re\{\mathbf{d}_5^H \mathbf{d}_6\} = 0. \end{aligned} \quad (38)$$

The cross-path gain terms are:

$$\begin{aligned} I_{35} = I_{53} = I_{46} = I_{64} &= \frac{2}{\sigma_s^2} \Re\{\mathbf{d}_3^H \mathbf{d}_5\} = \\ &= \frac{2}{\sigma_s^2} \Re\left\{ \sum_{n \in K_s} |a_s[n]|^2 e^{-j2\pi f[n](\tau_2 - \tau_1)} \right\}, \\ I_{36} = I_{63} &= \frac{2}{\sigma_s^2} \Re\{\mathbf{d}_3^H \mathbf{d}_6\} = \\ &= -\frac{2}{\sigma_s^2} \Im\left\{ \sum_{n \in K_s} |a_s[n]|^2 e^{-j2\pi f[n](\tau_2 - \tau_1)} \right\}, \\ I_{45} = I_{54} &= \frac{2}{\sigma_s^2} \Re\{\mathbf{d}_4^H \mathbf{d}_5\} = \\ &= \frac{2}{\sigma_s^2} \Im\left\{ \sum_{n \in K_s} |a_s[n]|^2 e^{-j2\pi f[n](\tau_2 - \tau_1)} \right\}. \end{aligned} \quad (39)$$

All remaining gain-gain entries follow by symmetry.

E. Delay-Gain Mixed Terms

The mixed terms are:

$$\begin{aligned} I_{13} = I_{31} &= \frac{2}{\sigma_s^2} \Re\{\mathbf{d}_1^H \mathbf{d}_3\} = \frac{4\pi}{\sigma_s^2} \alpha_{1\text{Im}} \sum_{n \in K_s} |a_s[n]|^2 f[n], \\ I_{14} = I_{41} &= \frac{2}{\sigma_s^2} \Re\{\mathbf{d}_1^H \mathbf{d}_4\} = -\frac{4\pi}{\sigma_s^2} \alpha_{1\text{Re}} \sum_{n \in K_s} |a_s[n]|^2 f[n], \\ I_{25} = I_{52} &= \frac{2}{\sigma_s^2} \Re\{\mathbf{d}_2^H \mathbf{d}_5\} = \frac{4\pi}{\sigma_s^2} \alpha_{2\text{Im}} \sum_{n \in K_s} |a_s[n]|^2 f[n], \\ I_{26} = I_{62} &= \frac{2}{\sigma_s^2} \Re\{\mathbf{d}_2^H \mathbf{d}_6\} = -\frac{4\pi}{\sigma_s^2} \alpha_{2\text{Re}} \sum_{n \in K_s} |a_s[n]|^2 f[n]. \end{aligned} \quad (40)$$

The separation-dependent mixed terms are:

$$\begin{aligned} I_{15} = I_{51} &= \frac{2}{\sigma_s^2} \Re\{\mathbf{d}_1^H \mathbf{d}_5\} = \frac{4\pi}{\sigma_s^2} \Re\left\{ (\alpha_{1\text{Im}} + j\alpha_{1\text{Re}}) \right. \\ &\quad \left. \times \sum_{n \in K_s} |a_s[n]|^2 f[n] e^{-j2\pi f[n](\tau_2 - \tau_1)} \right\}, \\ I_{16} = I_{61} &= \frac{2}{\sigma_s^2} \Re\{\mathbf{d}_1^H \mathbf{d}_6\} = \frac{4\pi}{\sigma_s^2} \Re\left\{ (\alpha_{1\text{Re}} - j\alpha_{1\text{Im}}) \right. \\ &\quad \left. \times \sum_{n \in K_s} |a_s[n]|^2 f[n] e^{-j2\pi f[n](\tau_2 - \tau_1)} \right\}, \end{aligned} \quad (41)$$

$$\begin{aligned} I_{23} = I_{32} &= \frac{2}{\sigma_s^2} \Re\{\mathbf{d}_2^H \mathbf{d}_3\} = \frac{4\pi}{\sigma_s^2} \Re\left\{ (\alpha_{2\text{Im}} + j\alpha_{2\text{Re}}) \right. \\ &\quad \left. \times \sum_{n \in K_s} |a_s[n]|^2 f[n] e^{+j2\pi f[n](\tau_2 - \tau_1)} \right\}, \\ I_{24} = I_{42} &= \frac{2}{\sigma_s^2} \Re\{\mathbf{d}_2^H \mathbf{d}_4\} = \frac{4\pi}{\sigma_s^2} \Re\left\{ (\alpha_{2\text{Re}} - j\alpha_{2\text{Im}}) \right. \\ &\quad \left. \times \sum_{n \in K_s} |a_s[n]|^2 f[n] e^{+j2\pi f[n](\tau_2 - \tau_1)} \right\}. \end{aligned} \quad (42)$$

Collecting all entries gives the 6×6 FIM.

F. Remarks on Frequency Centering

When the carrier frequency grid is centered, the sum $\sum_{n \in K_s} |a_s[n]|^2 f[n]$ can be close to zero, which reduces the influence of the linear frequency sum in delay-gain mixed FIM entries presented in (40). Under that condition, the multiband configuration enters mainly through quadratic frequency sums and through the weighted phase term $e^{-j2\pi f[n](\tau_2 - \tau_1)}$, which governs the CRLB dependence on $\Delta\tau$.

REFERENCES

- [1] M. A. Saeidi, H. Tabassum, and M.-S. Alouini, "Multi-band wireless networks: Architectures, challenges, and comparative analysis," *IEEE Communications Magazine*, vol. 62, no. 1, pp. 80–86, 2023.
- [2] S. Aboagye, M. Amin Saeidi, H. Tabassum, Y. Tayyar, E. Hossain, H.-C. Yang, and M.-S. Alouini, "Multi-band wireless communication networks: Fundamentals, challenges, and resource allocation," *IEEE Transactions on Communications*, vol. 72, no. 7, pp. 4333–4383, 2024.
- [3] M. Rasti, S. K. Taskou, H. Tabassum, and E. Hossain, "Evolution toward 6g multi-band wireless networks: A resource management perspective," *IEEE Wireless Communications*, vol. 29, no. 4, pp. 118–125, 2022.
- [4] E. Khorov, I. Levitsky, and I. F. Akyildiz, "Current status and directions of IEEE 802.11be, the future wi-fi 7," *IEEE Access*, vol. 8, pp. 88 664–88 688, 2020.
- [5] L. Galati-Giordano, G. Geraci, M. Carrascosa, and B. Bellalta, "What will wi-fi 8 be? a primer on IEEE 802.11 bn ultra high reliability," *IEEE Communications Magazine*, vol. 62, no. 8, pp. 126–132, 2024.
- [6] T. Kazaz, G. J. Janssen, J. Romme, and A.-J. Van der Veen, "Delay estimation for ranging and localization using multiband channel state information," *IEEE Transactions on Wireless Communications*, vol. 21, no. 4, pp. 2591–2607, 2021.
- [7] J. Pegoraro, J. O. Lacruz, M. Rossi, and J. Widmer, "Hisac: high-resolution sensing with multiband communication signals," in *Proceedings of the 22nd ACM Conference on Embedded Networked Sensor Systems*, 2024, pp. 549–563.
- [8] Z. Xiao, Z. Zhou, Q. Dai, Y. Zeng, F. Yang, and Y. Chen, "Achieving full-bandwidth sensing performance with partial bandwidth allocation for isac," *IEEE Wireless Communications Letters*, 2025.
- [9] S. Kato, P. Wang, T. Koike-Akino, T. Fujihashi, H. Mansour, and P. Boufounos, "Multi-band wi-fi neural dynamic fusion," *IEEE Transactions on Wireless Communications*, 2025.
- [10] A. Jeknić, A. Švigelj, T. Javornik, and A. Hrovat, "Effects of non-contiguous spectrum on time-of-arrival estimation in multiband isac," in *2025 International Conference on Software, Telecommunications and Computer Networks (SoftCOM)*. IEEE, 2025, pp. 1–5.
- [11] J. A. Armenta-Garcia, F. F. Gonzalez-Navarro, and J. Caro-Gutierrez, "Wireless sensing applications with wi-fi channel state information, pre-processing techniques, and detection algorithms: A survey," *Computer Communications*, vol. 224, pp. 254–274, 2024.
- [12] Z. Li, C. Chen, J. Zhang, C. R. Da Silva, O. Yurduseven, T. Q. Duong, and S. L. Cotton, "Sensing line of sight perturbations in 6 ghz wi-fi using channel model based features," *IEEE Sensors Journal*, 2025.

- [13] J. Ding, Y. Wang, J. Zhang, H. Chen, H. Si, and J. Liu, "Multi-ap csi fusion and features optimization-based behavioral sensing on wifi platform," *IEEE Sensors Journal*, vol. 23, no. 22, pp. 27 601–27 612, 2023.
- [14] P. Picazo-Martinez, C. Barroso-Fernández, A. Calvillo-Fernandez, M. Groshev, C. J. Bernardos, A. de la Oliva, and A. Mourad, "802.11 bf multiband passive sensing: Reusing wi-fi signaling for sensing," *IEEE Internet of Things Journal*, 2026.
- [15] S. Dimce and F. Dressler, "Survey on coherent multiband splicing techniques for wideband channel characterization," *IET Communications*, vol. 18, no. 19, pp. 1319–1334, 2024.
- [16] S. Dimce, A. Zubow, A. Bayesteh, G. Caire, and F. Dressler, "Reconsidering sparse sensing techniques for channel sounding using splicing," *IEEE Transactions on Mobile Computing*, 2025.
- [17] K. Wu, J. Pegoraro, F. Meneghello, J. A. Zhang, J. O. Lacruz, J. Widmer, F. Restuccia, M. Rossi, X. Huang, D. Zhang *et al.*, "Sensing in bistatic isac systems with clock asynchronism: A signal processing perspective [special issue on signal processing for the integrated sensing and communications revolution]," *IEEE Signal Processing Magazine*, vol. 41, no. 5, pp. 31–43, 2024.
- [18] Y. Wan, Z. Hu, A. Liu, R. Du, T. X. Han, and T. Q. Quek, "Ofdm-based multiband sensing for isac: Resolution limit, algorithm design, and open issues," *IEEE Vehicular Technology Magazine*, 2024.
- [19] F. Meneghello, A. Blanco, A. Cusano, J. Widmer, and M. Rossi, "Wi-fi multi-path parameter estimation for sub-7 ghz sensing: A comparative study," in *2023 19th International Conference on Wireless and Mobile Computing, Networking and Communications (WiMob)*. IEEE, 2023, pp. 237–242.
- [20] H. Dun, C. C. Tiberius, C. Diouf, and G. J. Janssen, "Sparse signal bands selection for precise time-based ranging in terrestrial positioning," in *2020 IEEE/ION Position, Location and Navigation Symposium (PLANS)*, 2020, pp. 1372–1380.
- [21] Y. Wan, A. Liu, R. Du, T. X. Han, and T. Q. Quek, "Fundamental limits and optimization of multiband delay estimation in ofdm systems," *IEEE Internet of Things Journal*, vol. 11, no. 19, pp. 31 112–31 127, 2024.
- [22] S. M. Kay, *Fundamentals of statistical signal processing: estimation theory*. Prentice-Hall, Inc., 1993.
- [23] P. Stoica, R. L. Moses *et al.*, *Spectral analysis of signals*. Pearson Prentice Hall Upper Saddle River, NJ, 2005, vol. 452.
- [24] H. L. Van Trees and K. L. Bell, *Detection estimation and modulation theory, part I: detection, estimation, and filtering theory*. John Wiley & Sons, 2013.
- [25] E. L. Lehmann and G. Casella, *Theory of point estimation*. Springer, 1998.
- [26] IEEE, "IEEE Standard for Information Technology–Telecommunications and Information Exchange between Systems Local and Metropolitan Area Networks–Specific Requirements Part 11: Wireless LAN Medium Access Control (MAC) and Physical Layer (PHY) Specifications," IEEE Std 802.11-2024 (Revision of IEEE Std 802.11-2020), pp. 1–5956, 2025.